Cold Regions Science and Technology 181 (2021) 103196

Contents lists available at ScienceDirect

Cold Regions Science and Technology

journal homepage: www.elsevier.com/locate/coldregions

An experimental study of rain erosion effects on a hydro-/ice-phobic coating pertinent to Unmanned-Arial-System (UAS) inflight icing mitigation

Zichen Zhang [a], Liqun Ma [a], Yang Liu [a], Juan Ren [b], Hui Hu [a,*]

[a] Department of Aerospace Engineering, Iowa State University, Ames, IA 50011, USA
[b] Department of Mechanical Engineering, Iowa State University, Ames, IA 50011, USA

ARTICLE INFO

Keywords:
Rain erosion effects
Superhydrophobic surface
Surface wettability
Icephobicity

ABSTRACT

An experimental investigation was conducted to evaluate the variations of the surface wettability and ice adhesion strength on a typical hydro−/ice-phobic surface before and after undergoing continuous impingement of water droplets (i.e., rain erosion effects) at relatively high speeds (i.e., up to ~100 m/s) pertinent to Unmanned-Arial-System (UAS) inflight icing mitigation. The experimental study was conducted by leveraging a specially designed rain erosion testing rig available at Iowa State University. Micro-sized water droplets carried by an air jet flow were injected normally onto a test plate coated with a typical Super-Hydrophobic Surface (SHS) coating to simulate the scenario with micro-sized water droplets in the cloud impacting onto UAS airframe surfaces. During the experiments, the surface wettability (i.e., in the terms of static, advancing and receding contact angles of water droplets) and the ice adhesion strength on the SHS coated test plate were quantified as a function of the duration of the rain erosion testing. The surface topology changes of the SHS coated surface against the duration of the rain erosion testing were also measured by using an Atomic Force Microscope (AFM) system. The characteristics of the surface wettability and ice adhesion strength on the eroded SHS surface are correlated with the AFM measurement results to elucidate the underlying physics for a better understanding about the rain erosion effects on hydro−/ice-phobic coatings in the context of UAS inflight icing mitigation.

1. Introduction

Unmanned Aerial System, i.e., UAS in short, is one of the most remarkable developments in aviation community in recent years. These remotely or sometimes autonomously controlled aerial vehicles have become invaluable tools for various civilian and military applications. Free from having to accommodate the safety needs and endurance limits of onboard pilots, UAS is capable of flying extended missions and venturing into hazardous and remote locations (Miziński and Niedzielski, 2017). Additionally, the associated cost savings and casualty reduction in using UAS for various military reconnaissance and surveillance operations are also very attractive, in comparison to conventional manned aircraft. As a result, military operations have seen a widespread use of UAS, such as Global Hawk, Predator and Phoenix.

Inflight icing is a common aviation danger that plagues both unmanned and manned airplanes flying in cold climate (Cao et al., 2018). In comparison to conventional manned aircraft, the small-scale, light-weighted UAS is much more susceptible to icing problems due to the lower cruising altitude with relatively higher liquid water content (LWC) and warmer air temperatures, smaller excess power margin to offset the increased drag caused by ice accretion, lower flying velocity to result in much longer exposing to icing conditions, and more vulnerable to cause damages to important sensors onboard. The potential damage of inflight icing to UAS renders their operation unfeasible in cold weather. As described in Botura and Fahrner (2003), 25% UAS flights encountered icing during a specific military operation that have negatively impacted the success of the mission. The common UAS icing avoidance strategies are keeping UAS on the ground or modifying path planning (Zhang et al., 2014) which would greatly reduce UAS operation capability in cold climate. This is particularly troublesome for military applications, in which icing conditions can lead to aborted missions and the loss of crucial tactical capabilities.

Extensive efforts have been undertaken in recent years to develop anti−/de-icing methods for aircraft icing protection/mitigation (Brown

* Corresponding author.
E-mail address: huhui@iastate.edu (H. Hu).

https://doi.org/10.1016/j.coldregions.2020.103196
Received 18 April 2020; Received in revised form 17 September 2020; Accepted 27 October 2020
Available online 31 October 2020
0165-232X/© 2020 Elsevier B.V. All rights reserved.

et al., 2002; Liu et al., 2017; Parent and Ilinca, 2011; Thomas et al., 1996). While anti-icing refers to the prevention of any buildup of ice structures on a surface, de-icing denotes the case where ice has already formed on a surface, which is subsequently removed. Almost all the anti−/de-icing methods currently used for aircraft inflight icing mitigation can be classified in two categories: active and passive methods. While active methods rely on supplying external energy to the system for anti−/de-icing operation, passive methods take advantage of the physical properties of airframe surfaces to prevent or suppress ice formation/accretion. Currently, the most-commonly-used anti−/de-icing approaches for aircraft inflight icing protection are thermal-based systems, i.e., utilizing electric resistant heating, hot air bleeding, or microwave heating to warm up airframe surfaces to melt out accreted ice structures, and have been successfully implemented on large-scale, manned aircraft (Cao et al., 2018). However, those anti−/de-icing measures can be too complex, too heavy or draw too much power to be effective, therefore, will not be applicable to small-scale, light weighted UAS due to the limited payload and scant excess power (Muthumani et al., 2014). Passive anti-icing approaches using hydro−/ice-phobic surface coatings are currently being investigated for use as viable strategies for aircraft icing mitigation (Antonini et al., 2011; Kulinich and Farzaneh, 2011). An ideal solution for UAS inflight icing mitigation would be a hybrid system that requires only a minimized power input to effectively delaminate the ice accretion in the required locations, while utilizing passive hydro−/ice-phobic coatings with ultra-low ice adhesion strength and good mechanical durability to reject ice accretion with the requisite aerodynamic forces (Gao et al., 2019; Ma et al., 2020).

Inspired by the outstanding self-cleaning capability of lotus leaf or duck feather (Feng et al., 2002; Lv et al., 2014), a number of studies have been conducted in recent years to develop coatings to make superhydrophobic surfaces (SHS), on which water droplets bead up with a very large contact angle (i.e., $> 150°$) and drip off rapidly when the surface is slightly inclined. One attractive application of SHS, in addition to the extraordinary water-repellency, is their potentials to reduce accumulation of snow and ice on solid surfaces. Under a frost-free environment (e.g., low humidity conditions), SHS has been found to show promising behaviors in delaying ice formation (Cao et al., 2009; Tourkine et al., 2009), even at temperatures as low as −30 °C (Mishchenko et al., 2010).

It is well known that the hydrophobicity of a surface usually results from a combination of chemical hydrophobicity with micro−/−nano-textured surface (Antonini et al., 2014; Dorrer and Rühe, 2009). As shown in Fig. 1, SHS repels water droplets by maintaining a non-wetting ***Cassie-Baxter state*** of water sitting on the top of micro−/nano-scale roughness/textures, with an air layer filling the roughness voids (Cassie and Baxter, 1944; Yao et al., 2011). The large contact angles (CA) and small contact angle hysteresis (CAH, which is defined as the difference between the advancing and receding contact angles) result in extremely low adhesion stresses acting between the water and the surface. Consequently, only very small forces tangent to the surface are required to mobilize the water droplets (Deng et al., 2012; Li et al., 2007). However, the water droplets sitting on the micro-scale textured surfaces can also transition to the fully wetted state, i.e., ***Wenzel state***, under sufficient external forcing. As a result, the water can be pushed into the surface roughness, displacing the air and fully wetting the surface in the Wenzel state (Nosonovsky, 2011).

While SHS coatings with micro−/nano-scale surface textures were reported to show promising performance in suppressing ice formation/accretion, almost all the previous tests were conducted in a relatively static environment (i.e., by handily spraying water droplets or pouring water onto SHS coated substrates and then freezing the test samples in refrigerators) to demonstrate their icephobic performance (Maitra et al., 2014; Varanasi et al., 2010). Very little work has been done to evaluate their icephobic capabilities for "*impact icing*" mitigation pertinent to UAS inflight icing phenomena under either dry rime or wet glaze icing condition(Gao et al., 2019; Liu et al., 2018). Here, the "*impact icing*" is defined as ice formed due to the dynamic collision of water droplets onto a cold surface at a high impacting velocity. The structure of impact ice accretion can vary considerably depending upon the conditions in which the ice is formed. Ambient temperature, airflow speed, water droplet size, liquid water content (LWC) in the airflow, and geometry of the airframe surfaces will all affect the ice structure that accretes.

For a representative case of UAS inflight icing scenario, super-cooled water droplets would impact onto the airframe surfaces at high impacting speeds of ~100 m/s or higher. The impinged water droplets would readily penetrate into the micro−/nano-scale surface textures, i.e., transition from the partially-wetted *Cassie-Baxter state* to the fully-wetted *Wenzel state*, thereby, eliminating the hydrophobicity of the

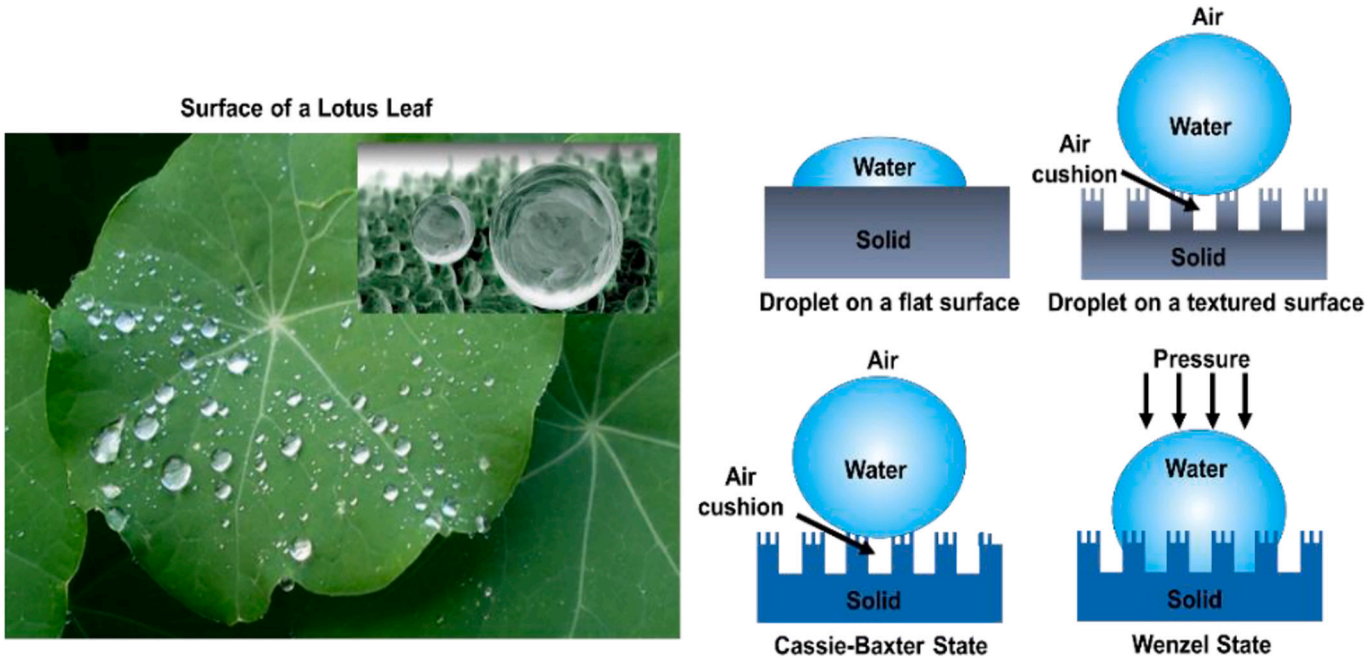

Fig. 1. Schematics of bio-inspired superhydrophobic surface (SHS).

surface (Nosonovsky, 2011). Once water freezes within the textures in the *Wenzel state*, it would very difficult to remove the ice, even more than on non-textured surfaces, because of the interlocking between ice and the textures (Lv et al., 2014; Nosonovsky and Hejazi, 2012; Sarshar et al., 2013). Furthermore, since UAS airframe surfaces would be exposed to the high-speed impingement of water droplets for a relatively long time, the "rain erosion" resistance performance of hydro−/ice-phobic coatings (i.e., the ability to prevent the material wearing away of the surface coatings from the substrates caused by the continuous high-speed impingement of water droplets) would also be very critical in considering a practical usage of hydro−/ice-phobic coatings to mitigate ice accretion over UAS airframe surfaces. It should also be noted that, while a number of previous studies were conducted to investigate rain erosion effects on surface coatings (Dear and Field, 1988; Fujisawa et al., 2018; Sharifi et al., 2019; Valaker et al., 2015), majority of those studies focused on mass loss of the coating materials caused by rain erosion effects, very little can be found in literature to study the degradation of surface wettability and ice adhesion strength changes due to the rain erosion effects. While SHS coatings were found to lose their super-hydrophobicity even for the test cases with relatively low droplet impacting velocity (i.e., ~ 10 m/s) (Tarquini et al., 2014; Yeong et al., 2014), systematic investigations to assess rain erosion effects on the surface wettability and ice adhesion characteristics of SHS coatings undergoing continuous impingement of water droplets at relatively high impacting velocity (i.e., up to ~100 m/s) pertinent to UAS icing phenomena have not been explored.

In the present study, a comprehensive experimental campaign was conducted to evaluate the variations of the surface wettability and ice adhesion strength on a typical hydro−/ice-phobic surface before and after undergoing continuous impingement of water droplets (i.e., rain erosion effects) at relatively high speeds (i.e., up to ~100 m/s) pertinent to UAS inflight icing mitigation. The experimental study was conducted by leveraging a specially-designed rain erosion testing rig available at Iowa State University to generate an air jet flow (i.e., up to ~100 m/s) laden with micro-sized water droplets at different liquid water content (*LWC*) levels. The micro-sized water droplets carried by the air jet flow would be impinging normally onto a test plates coated with a typical SHS coating to simulate the scenario of airborne, micro-sized water droplets in the cloud impacting onto UAS airframe surfaces. In the context that follows, the experimental setup used in the present study for the rain erosion testing and preparation of the SHS coated test surface along with the measurement techniques/systems to be used to quantify the surface wettability and the ice adhesion strength over the test surface during the course of the rain erosion testing will be described at first. After a brief introduction of the fundamental mechanisms of "rain erosion damages" to a solid surface, the measurement results of the rain erosion testing experiments will be presented. Comprehensive analysis and discussions will also be presented to evaluate the rain erosion effects on the SHS coating under various test conditions in the context to utilize hydro−/ice-phobic coatings for UAS inflight icing mitigation.

2. Experimental setup and preparation of the SHS coated test plate

2.1. A brief introduction of the rain erosion testing rig

As shown schematically in Fig. 2, a specially-designed rain erosion testing rig available at Aerospace Engineering Department of Iowa State University was used to evaluate rain erosion effects on a typical SHS coating undergoing continuous impingement of water droplets at relatively high impacting speeds up to ~100 m/s. A high-thrust electric ducted fan (EDF, JP Hobby) is installed at the inlet of a circular-shaped wind tunnel to drive airflow into the test rig. By manipulating the power supplied to the electric fan, the speed of the airflow exhausted from the nozzle of the wind tunnel (D_{nozzle} = 38 mm) can be adjusted, i.e., from 45 m/s to 95 m/s for the present study. While a water spray nozzle (BIMV-11002 nozzle) is integrated in the middle section of the wind tunnel, de-ionized water is supplied to the spray nozzle to generate micro-sized water droplets and inject them into the airflow. By manipulating the water flow rate supplied to the spray nozzle, the liquid water content (*LWC*) levels in the air jet flow can be varied for different testing conditions. By changing the pressure settings of the air and water

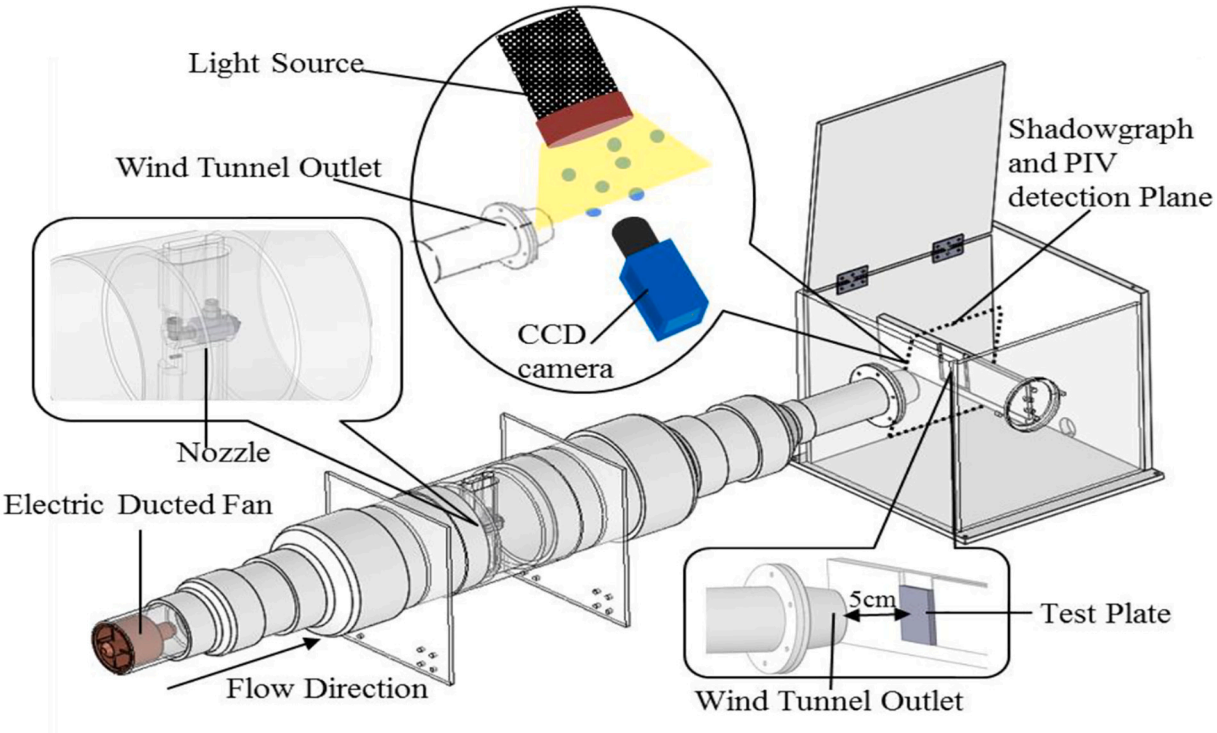

Fig. 2. Schematic of the rain erosion testing rig used in the present study.

supplying pipelines connected to the water spray nozzle, the size of the water droplets exhausted from the spray nozzle is also adjustable for different applications.

2.2. A typical SHS coating studied in the present study

A set of square-shaped aluminum plates with 50 mm in width and 6.5 mm in thickness were used as the test plates in the present study. Before applying a commercially-available SHS coating - Hydrobead® onto the test plates, the surfaces of the test plates were polished with sandpaper grits ranging from 220 to 2000 according to ASTM standards (E3-11) (Beeram et al., 2017). The pretreatment could strengthen the bond between SHS coating and the substrates as well as enhance the homogeneity of the SHS coating. Following the procedure suggested by the coating manufacturer, both Hydrobead® standard and Hydrobead® enhancer were applied onto the surfaces of the test plates. The thickness of the SHS coating sprayed on the test surfaces was found to be about 25 μm as measured by using a wet film gauge. Fig. 3 shows typical images of water droplets on a test plate before and after applying the SHS coating. It can be seen clearly that, before applying the SHS coating, the static contact angle of the sessile water droplet was found to be only ~65°. As revealed from the Scanning Electron Microscope (SEM) image for the SHS coated test surface given in Fig. 3(b), micro−/nano-scale surface textures were found to be generated after applying the Hydrobead® coating onto the test plate. In addition to its hierarchical polymeric superhydrophobic shell on the surface, fluorinated compounds in the Hydrobead® coating will also provide promise to achieve the superhydrophobicity. As a result, the static contact angle of a sessile water droplet on the SHS coated test surface was found to be about 156°, indicating that the Hydrobead® coated test surface is indeed superhydrophobic.

2.3. Measurements of the contact angles and ice adhesion strength on the test surfaces

In the present study, the changes of the surface wettability of the SHS coated test plate (i.e., in the terms of static contact angles (CA), θ_{static}; advancing CA, $\theta_{adv.}$; and receding CA, θ_{rec}, of water droplets on the test surfaces) as a function of the duration of the rain erosion testing were quantified by using a needle-in-the-sessile-drop method similar as that described in Korhonen et al. (2013). Fig. 4 gives the experimental setup used in the present study. While the static CA, θ_{static}, were measured by placing sessile water droplets (~50 μL deionized water in volume) on the test plate, the advancing CA, $\theta_{adv.}$ and receding CA, $\theta_{rec.}$ were measured by expanding and contracting the water droplets with a rate of 10 μL/s. The expanding and contracting of the water droplets were controlled by using a programmable Syringe pump (Genie Touch™). A digital camera (PCO2000 with 2000 pixels × 2000 pixels in spatial resolution) with a 12× zoom lens system (LaVision) was used to record the images of the water droplets siting on the SHS coated test plate in order to determine the static and dynamic CAs. An "in-house" MATLAB-based image processing software package was used to extract the CA information from the recorded droplet images. The CA measurements were repeated 10 times for each case to minimize the random measurement errors. The CA measurement uncertainty was estimated to be ±5°.

Table 1 summarizes the measured static, receding and advancing angles of water droplets before and after applying the SHS coating onto a test plate. It can be seen clearly that, before applying the SHS coating, the static CA of water droplets on the uncoated test plate was found to be obviously smaller than 90° (i.e., $\theta_{static} \approx 65°$), confirming the hydrophilic nature of bare aluminum surface. The corresponding CAH value (i.e., the difference between the advancing and receding contact angles of the water droplets, $\Delta\theta = \theta_{adv} - \theta_{rec}$) was found to be bigger than 70°. In comparison, after applying the SHS coating, while the static CA of water droplets on the SHS coated test surface was found to become $\theta_{static} \approx$ 156°, the corresponding CAH value is only ~3°.

By using a similar measurement technique as the one described in Beemer et al. (2016) and Meuler et al. (2010), the variations of the ice adhesion strengths, τ_{ice}, on the test plate as a function of the duration of the rain erosion testing were also measured in the present study. With the similar experiment setup as that described in Beeram et al. (2017); the test plate undergoing different duration of the rain erosion testing was mounted in a temperature controlled test chamber for the ice adhesion measurements. For the test cases of the present study, while the surface temperature of the test plate was maintained at $T_w = -10$ °C, ice adhesion measurements were repeated ~10 times for each test cases. The uncertainty for the ice adhesion measurements was estimated to be ±20 kPa. The measured ice adhesion strengths on the test plate before and after applying the SHS coating are also listed in Table 1 for comparison. It can be seen that, the ice adhesion strength on the bare aluminum surface of the test plate (i.e., before applying the SHS coating) was found to be ~450 kPa, which is within the range of the values reported in Saleema et al. (2011) for bare aluminum surfaces. In comparison, the ice adhesion strength on the SHS coated surface (i.e., the newly prepared test surface before undergoing rain erosion testing) was found to become τ_{ice}, = ~ 105 kPa, which is only about ¼ of the corresponding value of the test case without applying the SHS coating. It confirms that the SHS coating used in the present study is also icephobic.

2.4. Surface topology measurements with an Atomic Force Microscopy (AFM) system

In the present study, the surface topology variations of the SHS coated test plate as a function of the duration of the rain erosion testing experiments were also characterized by using a high-resolution Atomic

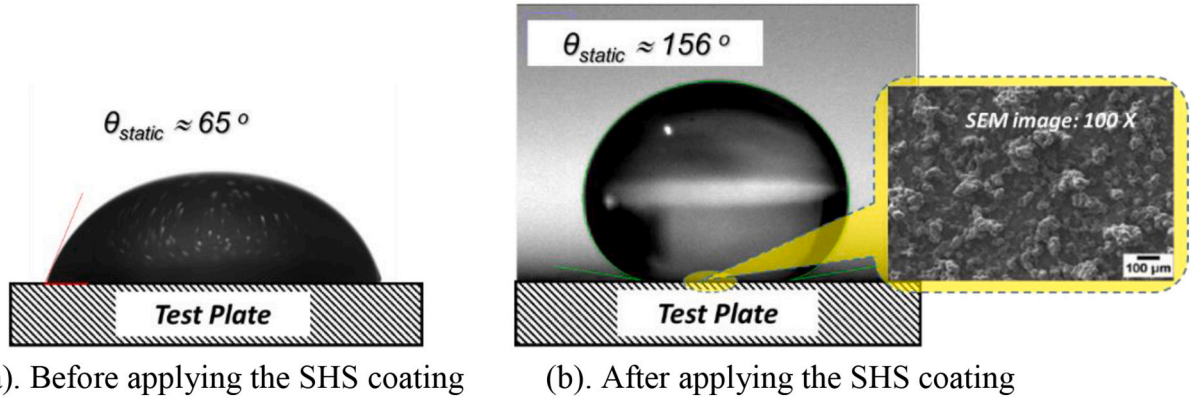

Fig. 3. Images of water droplets on the test plate before and after applying SHS coating.

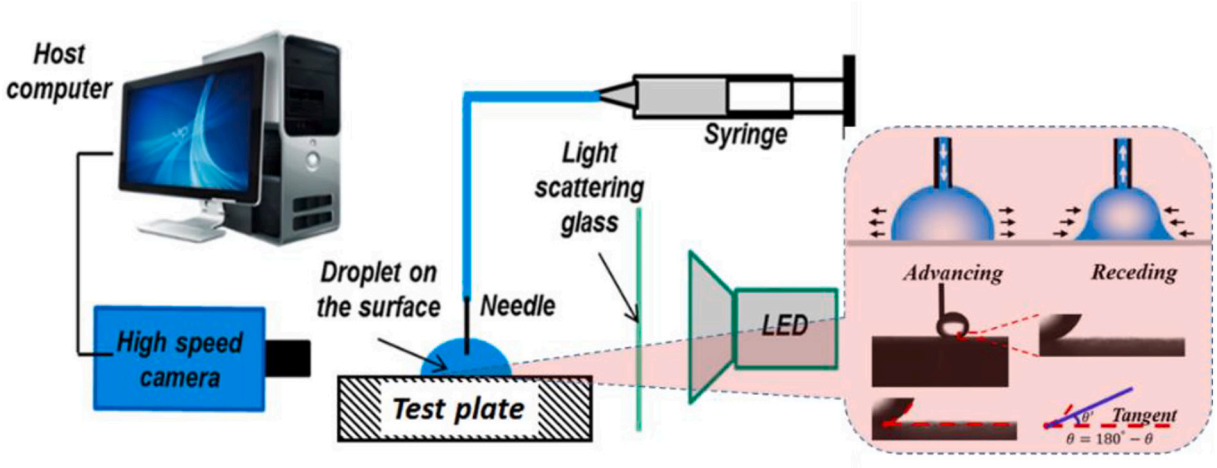

Fig. 4. The experimental setup to measure contact angles of droplets on the test surfaces.

Table 1
Measured contact angles and ice adhesion strength on the test plate.

Studied Surface	Wettability	Static CA θ_{static}	Advancing CA, θ_{adv}	Receding CA, θ_{rec}	Hysteresis Δθ	Ice adhesion strength (KPa)
Before applying the SHS coating on the test plate	Hydrophilic	~65°	~105°	~35°	>70°	~450
After applying the SHS coating on the test plate	Super-Hydrophilic	~156°	~163°	~160°	~ 3°	~105

Force Microscopy (AFM) system (Bioscope Resolve, Bruker Inc.) integrated with an inverted optical microscope (IX73, Olympus). The drive voltage, the piezo displacement data and cantilever deflection of the AFM probe were acquired using a DAQ board (National Instrument, PCIe-6353). An AFM probe (DNP, Bruker) with a nominal conical radius of 20 nm and an opening angle of 20 degree was used for the topographic imaging of the SHS coated test surface. Before characterizing of the topology of the test surface, the radius of the AFM probe radius was calibrated carefully by using a polycrystalline titanium roughness sample (Bruker Inc). While the AFM system was operated in the tapping mode, the cantilever spring constant for the AFM measurements was set as 0.03 N/m. The AFM probe was placed in contact with the SHS coated test surface to produce high-resolution topographical images, then lifted off from the test surface and moved to next measurement position. Further information about the AFM system used in the present study and the operation procedure for the AFM measurements can be found at Xie and Ren (2019) and Mollaeian et al. (2019).

3. Fundamental mechanism of the damages to a solid surface by "rain erosion effects"

The fundamental mechanism of "rain erosion" damages to a solid surface (i.e., surface damages caused by the continuous impingement of water droplets) is closely related to the impinging dynamic of water droplets (Jackson and Field, 2000). As described in Grundwürmer et al. (2007), the impinging dynamics of a droplet onto a solid surface can be divided into three stages: the first is the compressible stage where the liquid droplet is considered to be compressible due to the generation of a shockwave at the initial impinging zone with an extremely high "water hammer" pressure; the second is the impacting wave generation stage featured by the fast propagation of surface Rayleigh waves and bulk waves in a relatively large area; and the final one is the incompressible stage mainly involving in momentum transfer of the impinging droplet (Slot et al., 2015). As shown schematically in Fig. 5, while a shock wave is generated in the initial impinging zone highlighted in blue color, the longitudinal Rayleigh waves and transverse bulk waves are generated later and propagate along the surface and into the substrate, respectively.

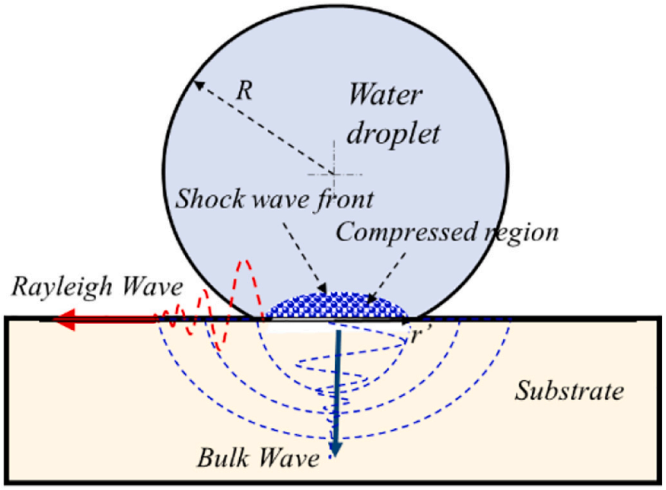

Fig. 5. Rain erosion mechanism after a droplet impacting onto a solid surface.

While water is usually considered to be incompressible, water droplet however, can be compressible at the initial stage of the impinging process, and a shock wave would be generated at the solid-liquid interface, as described in Slot et al. (2015). This phenomenon is called "water hammer effect", and the pressure generated in this stage is named as "water hammer pressure" (Fujisawa et al., 2018; Ghidaoui et al., 2005; Thomas and Brunton, 1970). The magnitude of the "water hammer pressure" is a function of the droplet impinging velocity as well as the physical properties of the liquid and solid (e.g., density and speed of sound), and can be expressed as:

$$P_{hammer} = \rho_L c_L U_\infty \left(\frac{1}{1 + (\rho_L c_L / \rho_S c_S)} \right) \quad (1)$$

where $\boldsymbol{U}_\infty$ is the impacting speed of the droplet, ρ_L and ρ_S are the density of the liquid and the solid substrate, c_L and c_S are the speed of sound in the liquid and solid, respectively.

It should be noted that, the "water hammer pressure" could be much higher than the dynamic pressure of an impinging water droplet. For example, for a water droplet impinging onto an aluminum surface at the impacting speed of $\boldsymbol{U}_\infty = 50$ m/s, while the droplet dynamic pressure is $P_{dynamic} = \rho \boldsymbol{U}_\infty^2 \approx 2.5$ MPa, the corresponding "water hamper pressure" can reach up to $P_{hammer} \approx 75$ MPa, which is about 30 times greater than the droplet dynamic pressure. According to Thomas and Brunton (1970), while the duration of the "water hammer effect" is ultra-short, i.e., on the order of nanoseconds, the radius of the area experiencing the "water hammer pressure" can be estimated by $r_{hammer} = RU_\infty/c$, where R is the droplet radius, and c is the sound speed in the liquid.

As shown schematically in Fig. 6, Rayleigh surface waves and bulk waves would also be generated and propagate immediately due to the sudden surface distortion caused by the droplet impacting (Blowers, 1969). Since the moving speed of the contact edge is much greater than the wave propagation speed at the initial stage of the droplet impacting process, the "water hammer effect" is much more violent, while the wave effects are of little importance in the compressible stage (Slot et al., 2015). However, as the droplet spreads over the solid surface, the moving speed of the contact edge would become slower and slower due to liquid viscosity and friction force given by the substrate. As a result, the Rayleigh and bulk waves would become dominant factors to cause material degradation at the second stage. According to Jackson and Field (2000), while bulk waves are more critical for thin specimen, Rayleigh surface waves would be more destructive for the thick test plate used in the present study (i.e. ~6.5 mm in thickness). As described in Blowers (1969), the stress level induced by Rayleigh surface waves can be estimated as:

$$P_{Rayleigh}(r) = \rho_L c_L U_\infty \left(\frac{1}{1+(\rho_L c_L/\rho_S c_S)}\right)\left(\frac{r_{hammer}}{\xi}\right)^{0.5} \quad (4)$$

where ξ is the distance to the impact center. Based on Eq. (2), for a water droplet impinging onto an aluminum surface at the impacting speed of $\boldsymbol{U}_\infty = 50$ m/s, the magnitude of the stress induced by Rayleigh surface waves would be about 40 MPa as the waves propagating to $\xi = 3r_{hammer}$, while the corresponding value for the bulk waves is only about 8 MPa.

At the end of the compressible stage, while the released waves would finally propagate to the contact line and neutralize the effects of the shock wave, the impact stress would decrease significantly, and the liquid would become incompressible (Slot et al., 2015). As described above, although the dynamic pressure of the impinging droplet is much smaller than the "water hammer pressure", the acting area of the dynamic pressure is much greater than that of the "water hammer pressure". As described in Thomas and Brunton (1970), while the effective area of the dynamic pressure for an impinging droplet can be estimated as πR^2, the effective area for the water hammer pressure is only $\pi(r_{hammer})^2 = \pi\ (R\ \boldsymbol{U}_\infty/c)^2$. More specifically, for a water droplet impinging onto a solid surface with the impacting velocity of $\boldsymbol{U}_\infty = 50$ m/s, the acting area of the dynamic pressure would be about 1000 times greater than that of the water hammer pressure. The significantly greater acting area of the dynamic pressure would lead to surface damages over a much larger area.

In summary, the damages to a solid surface caused by the dynamic impacting of liquid droplets can be categorized mainly at two levels (Thomas and Brunton, 1970). The first level occurs when the water droplet impacts onto the solid surface to initiate a deformation and first cracks due to the tremendous "water hammer pressure" at the initial stage of the impacting process, as shown schematically in Fig. 6(a). Then, the generation of the Rayleigh waves and bulk waves would induce high velocity of the lateral water jets to tear away any unevenness in the surface material to augment the damages to the solid surface (i.e., lateral jetting effects), as shown in Fig. 6(b). Fig. 6(c) illustrates how the cracks would become cavities due to the subsequent droplets impacting onto the surface, allowing for large pieces to become dislodged. In the case where the cavity does not propagate further into the substrate, shear failure may also occur to the tips of the prone material, as shown in Fig. 6(d).

4. Measurement results and Discussions

4.1. Quantification of the water spray flow exhausted from the rain erosion test rig

As aforementioned, by changing the pressure settings of the air and water supplying pipelines connected to the water spray nozzle mounted in the middle section of the rain erosion test rig, the size of the water droplets exhausted from the spray nozzle is adjustable. In the present study, the size distribution of the water droplets exhausted from the wind tunnel nozzle of the rain erosion test rig was monitored by using a LaVision's ParticleMaster™ imaging system, which composes of a high-speed digital camera (PhotronFastCam MINI WX100) to record the shadow images of water droplets along with a bright backlight iumillation provided by a high-speed pulsed LED lamp (MiniConstellation). The droplet images are then analyzed by LaVision ParticleMaster™

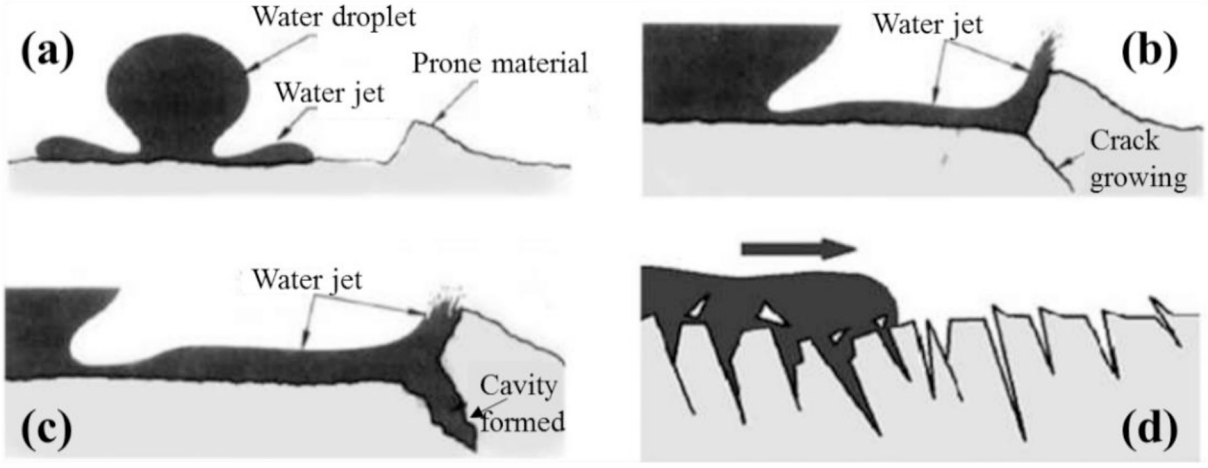

Fig. 6. Schematics of the damaging process due to rain erosion effect. (a). initiating a deformation and first cracks due to the tremendous "water hammer pressure" at the initial stage of the droplet impacting process; (b). Subsequent water jetting effects induced by the Rayleigh surface waves, pushing prone material, and creating cracks; (c). Crack propagating into a cavity; (d). Shear failure of prone materials. Reprint from Heyman (1970).

software to obtain the statistics of the water droplets, e.g., size distribution and mean size diameter. In order to simulate the rain erosion effects caused by the micro-sized, airborne water droplets in the cloud impacting onto UAS airframe surfaces, the size of the water droplets exhausted from the water spray nozzle was set to range from 10 μm to 100 μm with a median volumetric diameter (MVD) being about 20 μm for the test cases of the present study.

In the present study, a high-resolution digital particle image velocimetry (PIV) system was used to quantify the flying speed of the water droplets after exhausted from the nozzle of the wind tunnel. Fig. 7(a) shows a typical PIV raw image of the water droplets laden in the airflow with the freestream airflow velocity of $U_\infty = 95$ m/s, while Fig. 7(b) gives the velocity distribution of the flying water droplets derived from the acquired PIV images. The transverse velocity profiles of the water droplets exhausted from the wind tunnel nozzle under different test conditions (i.e., with the airflow velocity ranging from 45 m/s to 95 m/s) were shown in Fig. 7(c). It can be seen clearly that, the velocity of the flying water droplets was found to be rather uniform within the water spray flow and have almost the same velocity as the freestream airflow velocity (i.e., U_∞). Therefore, the freestream airflow velocity, U_∞, is referred as the nominal impacting velocity of the water droplets in the present study. Fig. 7(d) reveals the variations of the flying velocity of the water droplets along the spray flow direction as they approach to the test plate. It can be seen clearly that, due to the existence of a strong adverse pressure gradient near the impingement point, the water droplets were found to decelerate as approaching to the test plate, as expected. Upon continuous impingement of the water droplets onto the test plate, the rain erosion characteristics of the hydro−/ice-phobic coating on the test plate are examined under different test conditions.

During the rain erosion testing, while the water flowrate supplied to the spray nozzle was kept at a constant value (i.e., $\dot{Q}$=4.0 l/h), the wind speed of the airflow exhausted from the wind tunnel nozzle was varied from $\boldsymbol{U}_\infty = 45$ m/s to $\boldsymbol{U}_\infty = 95$ m/s for different test cases. As a result, the corresponding liquid water content (*LWC*) levels in the airflow would be different as the speed of the airflow changes. Table 2 summarizes the *LWC* level in the airflow under different rain erosion testing conditions. It can be seen clearly that, the *LWC* level in the airflow would change from $LWC \approx 21.7$ g/m^3 for the test case of $\boldsymbol{U}_\infty = 45$ m/s to $LWC \approx 10.3$ g/m^3 for the test case of $\boldsymbol{U}_\infty = 95$ m/s. It should be noted that, in comparison to the *LWC* levels within typical UAS flight envelopes of $LWC < 2.0$ g/m^3, the rain erosion testing cases of the present study were designed intentionally with much higher *LWC* levels (i.e., about 10 times higher) in order to accelerate the degradation of the hydro−/ice-phobic coating caused by the rain erosion effects.

Table 2
The *LWC* levels in the airflow under different rain erosion testing conditions.

Airflow speed, U_∞, (*m/s*)	45	55	65	75	85	95
LWC level in the airflow, (g/m^3)	21.7	17.7	15.0	13.0	11.5	10.3

As summarized in (Slot et al., 2015), in addition to material properties and surface roughness of the solid substrate, a number of parameters relevant to droplet impinging dynamics, including droplet size and shape, impacting velocity, impacting angle, number of droplet impingement, also play very important roles in determining the resultant damages to solid surfaces due to the rain erosion effects. Since the rain erosion damages to a surface coating will be related directly to the accumulated effects of the continuous impingement of water droplets onto the test surface at the same spot. A new parameter, named as "count of droplet impingement", is defined in the present study to characterize the rain erosion effects under different test conditions. The count of droplet impingement, *N*, is referred as the number of duty cycles of the damages to the test surface due to the continuous droplet impingement at the same location on the test surface. As described in Thomas and Brunton (1970), while the effective impingement area of a droplet of *R* in radius can be estimated as πR^2, the count of the droplet impingement, *N*, for different rain erosion testing cases of the present study can be estimated by:

$$N = \frac{n\pi R^2}{S_{impingement}} = \frac{n\pi R^2}{S_{nozzle}} \tag{3}$$

Where *n* is the total number of the water droplets exhausted from the wind tunnel nozzle, S_{nozzle} is the exit area of the wind tunnel nozzle, which equals to the impingement area of the spray jet flow onto the test plate.

For a rain erosion testing case with a given *LWC* level and droplet

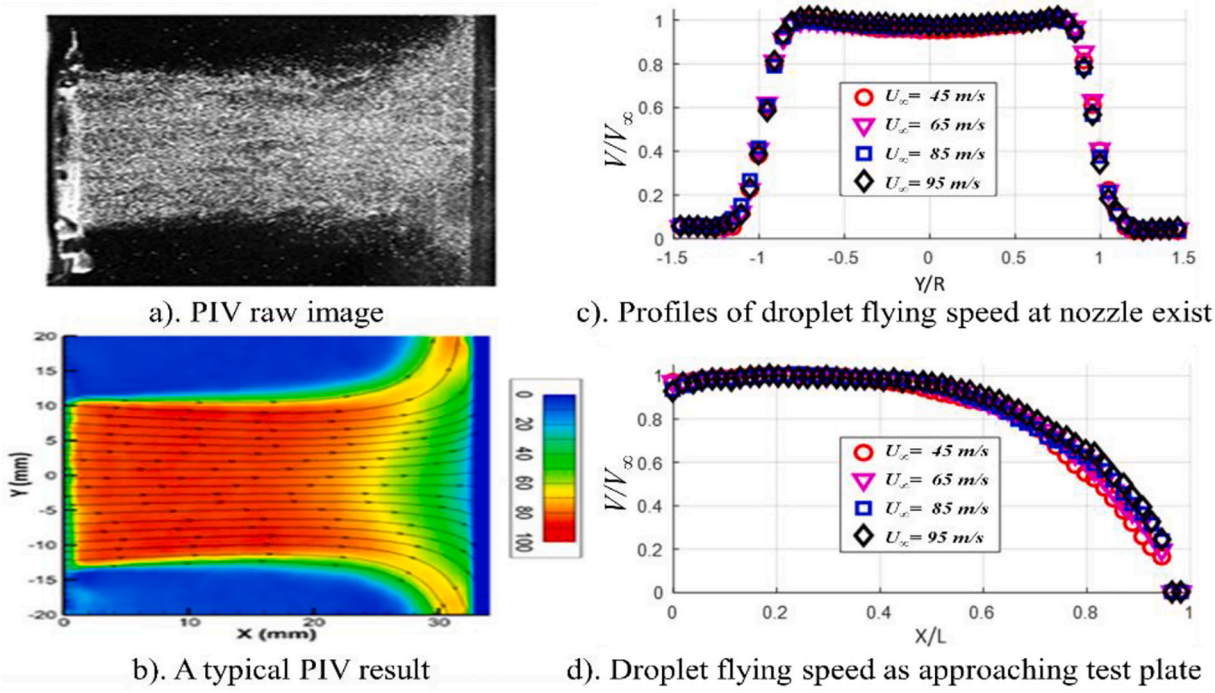

Fig. 7. PIV measurement results of the water spray flow before impacting onto the test plate.

impacting speed of U_∞, the total amount of the water mass exhausted from the wind tunnel nozzle can be calculated as $m_{water} = LWC \cdot U_\infty \cdot S_{nozzle} \cdot t$, where t is the duration of the rain erosion testing. As aforementioned, since the water droplets exhausted from the wind tunnel nozzle for the rain erosion testing have a median volumetric diameter (MVD) of ~20 μm (i.e., the averaged radius of $R \approx 10$ μm), the total number of the water droplets, n, can be estimated by taking the ratio between the total water mass exhausted from the wind tunnel nozzle to a mass of the individual water droplet:

$$n = \frac{m_{water}}{m_{droplet}} = \frac{3LWC \cdot t \cdot U_\infty \cdot S_{nozzle}}{4\rho\pi R^3} \tag{5}$$

Substituting n into Eq. (3), the count of the droplet impingement, N, can be expressed as:

$$N = \frac{3LWC \cdot U_\infty \cdot t}{4\rho R} \tag{6}$$

Under a given rain erosion testing condition, the count of the droplet impingement, N, would increase linearly with the duration of the rain erosion testing, t. Therefore, the count of the droplet impingement, N, could also be considered as the non-dimensional time to characterize the rain erosion damages to the SHS coated test surface.

4.2. Wettability degradation of the SHS coated test surface due to rain erosion effects

Figs. 8 and 9 present the measurement results of the rain erosion testing experiments to reveal the surface wettability degradation of the SHS coated test plate (i.e., in terms of static contact angles (CA), θ_{static}, advancing CA, $\theta_{adv.}$, and receding CA, θ_{rec}, of water droplets on the test surface) as a function of the duration of the rain erosion testing experiments. Since the count of droplet impingement, N, could also be considered as the non-dimensional time to characterize the rain erosion effects, the corresponding count of the droplet impingement, N, was also given in the plots as the second X-axis on the top of the plots. It can be seen clearly that, under the same rain erosion testing conditions (i.e., with the same LWC level in the airflow and droplet impacting speed of U_∞), both the static CA, θ_{static}, and the receding CA, θ_{rec}, were found to decrease monotonically with the increasing time of the rain erosion testing experiment (i.e., with more and more droplets impinging onto the test surface). However, the measured values of the advancing CA, θ_{adv} were found to stay almost at a constant value (i.e., $\theta_{adv} = 163° \pm 2°$)

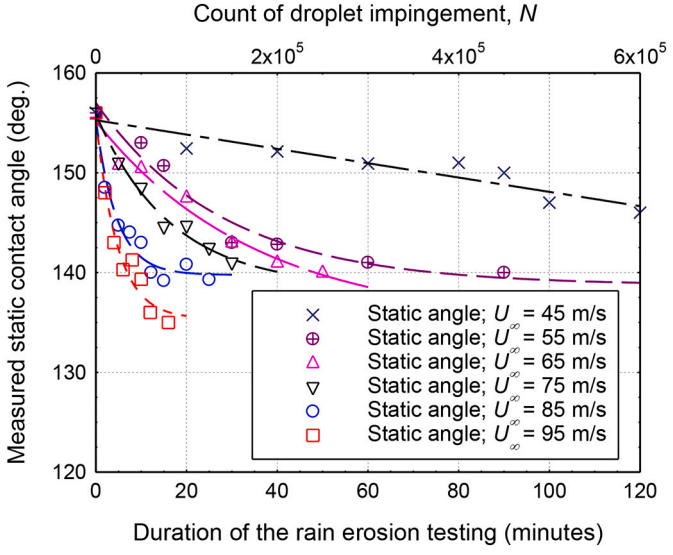

Fig. 8. Measured static contact angle, θ_{static}, vs. the time of the rain erosion testing.

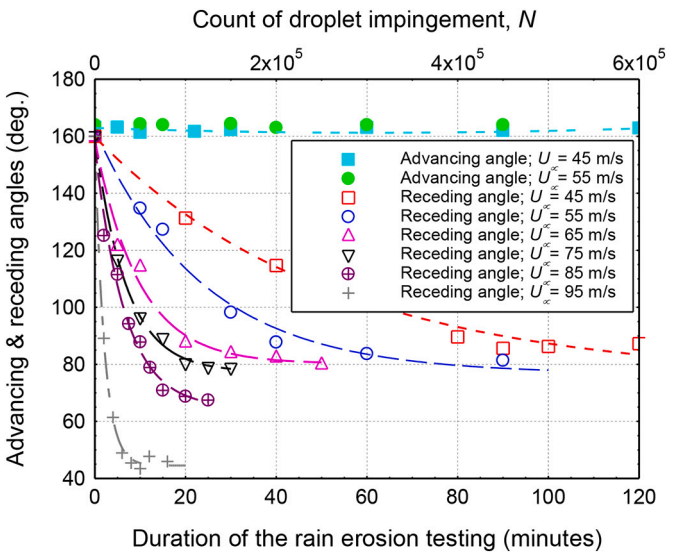

Fig. 9. Measured advancing & receding angles vs. the time of the rain erosion testing.

during the entire duration of the rain erosion testing experiments. It indicates that, the advancing CA is not sensitive to the changes of the surface textures/roughness caused by rain erosion effects, which agrees with the experimental findings reported by Zografi and Johnson (1984). It should also be noted that, the wettability degradation characteristics of the SHS coating (i.e., the time variations for both the measured static CA, θ_{static}, and the receding CA, θ_{rec} data) were found to be fitted reasonably well by using exponential functions, as shown by the dashed lines given in the plots.

The measurement results given in Fig. 8 and Fig. 9 also revealed clearly that, after undergoing the same number of the droplet impingement, wettability degradation of the SHS coated surface (i.e., the decreasing rates for both the static CA, θ_{static}, and the receding CA, θ_{rec}) was found to be much faster for the test cases with higher droplet impinging speed, in comparison to those with relatively lower droplet impacting speed. More specifically, for the test case with the nominal droplet impacting speed of $U_\infty = 45$ m/s, the measured static and the receding contact angles were found to decrease from their initial values of $\theta_{static} \approx 156°$ and $\theta_{rec} \approx 160°$ to $\theta_{static} \approx 146°$ and $\theta_{rec} \approx 82°$, respectively, after 120 min of the rain erosion testing (i.e., after about 600,000 times of the droplet impingement). However, as the nominal droplet impacting speed increases to $U_\infty = 95$ m/s, the corresponding static and the receding contact angles were found to become $\theta_{static} \approx 140°$ and $\theta_{rec} \approx 45°$, respectively, after a much shorter duration of the rain erosion testing of 20 min (i.e., after only about 100,000 times of the droplet impingement). It should be noted that the bare aluminum surface of the test plate (i.e., the bare test surface without the SHS coating) is hydrophilic with the static contact angles being only $\theta_{static} \approx 65°$. For the eroded SHS coated test surface, even though both the static CA, θ_{static}, and the receding CA, θ_{rec} were found to decrease substantially due to rain erosion efforts, the measured static contact angles on the eroded SHS coated surface were still found to be much greater than 90°. It indicates that the eroded SHS coated surface would still be hydrophobic due to the existence of a layer of the SHS coating material remaining on the surface of the test plate. However, the eroded SHS coated surface was found to loss its superhydrophobicity rapidly due to the grinding away of the hierarchical texture/roughness structures over the SHS coated surface after undergoing the rain erosion experiments, which will be revealed quantitatively in the later section to discuss the AFM measurement results.

4.3. The changes of ice adhesion strength on SHS coated surface due to rain erosion effects

As aforementioned, the variations of the ice adhesion strength on the SHS coated test plate as a function of the rain erosion testing duration were also measured under different testing conditions. Fig. 10 given the measurement results for the test case with the nominal droplet impacting speed of $U_\infty = 75$ m/s. The ice adhesion strength measurements were performed in a temperature-controlled test chamber with the surface temperature of the SHS coated test plate being set at $T_{surface} = -10.0$ °C. It can be seen clearly that, the ice adhesion strength on the SHS coated test plate was found to increase very rapidly at the earlier stage of the rain erosion testing (i.e., within the first 10 min), and then increase with much more moderate rates later as the time of the rain erosion testing increases. More specifically, while the ice adhesion strength on the SHS coated test surface was found to be $\tau_{ice} \approx 105$ kPa before starting the rain erosion testing, the corresponding value was found to increase to become $\tau_{ice} \approx 350$ kPa (i.e., ~ 3.5 times greater) after 10 min of the rain erosion testing (i.e., after ~50,000 times of droplet impingement) with the nominal droplet impacting speed of $U_\infty = 75$ m/s. After 30 min of the rain erosion testing (i.e., after ~150,000 times of droplet impingement), the ice adhesion strength on the SHS coated test surface was found to become $\tau_{ice} \approx 400$ kPa, which is slightly smaller than the value over bare aluminum surface (i.e., the test surface without SHS coating). It is also revealed clearly in Fig. 10 that the relationship between the measured ice adhesion strength data against the rain erosion testing duration would be fitted very well by using an exponential function. It should be noted that, after the rain erosion experiments, the SHS coating on the test plate was not completely grinded away, and the eroded SHS coated surface was still found to be icephobic with the static CA (i.e., $\theta_{static,} \approx 140°$) being much greater than that of the bare aluminum surface ($\theta_{static,} \approx 65°$). The significant increase of the ice adhesion strength over the eroded SHS coated surface is believed to be closely related to the vanishing of the hierarchical texture/roughness structures over the SHS coated surface due to the rain erosion effects, which will be discussed in further detail later based on the AFM measurement results.

It has been reported that, a hydrophobic material usually also displays lower ice adhesion strength in comparison to a hydrophilic material. This can be explained from a thermodynamic perspective by invoking the work of adhesion. The work of adhesion W_{adh} between ice and a solid material is given as, $W_{adh} = \gamma_{ia} + \gamma_{sa} - \gamma_{si}$, where γ_{ia} is ice surface energy (i.e., ice-air interfacial energy), γ_{sa} is the solid surface energy (i.e., solid-air interfacial energy) and γ_{si} is the solid-ice interfacial energy. Recognizing that the ice surface energy ($\gamma_{ia} = 75$ mJ/m^2) is approximately equal to the water surface energy (or surface tension, $\gamma_{wa} = 72$ mJ/m^2) and assuming that the ice-surface interfacial energy γ_{si} is approximately equal to the water-surface interfacial energy γ_{sw}, the work of adhesion can be rewritten as $W_{adh} \approx \gamma_{wa} + \gamma_{sa} - \gamma_{sw}$(Makkonen, 2012; Makkonen, 1997; Meuler et al., 2010). The hydrophobicity or hydrophilicity of a non-textured solid material is given by the Young's equation as$\gamma_{wa} \cos\theta_Y = \gamma_{sa} - \gamma_{sw}$, where θ_Y is the Young's contact angle of water on the solid surface. By combining the Young's equation with the work of adhesion, $W_{adh} \approx \gamma_{wa}(1 + cos\ \theta_Y)$ can be obtained. This equation is known as Young-Dupre equation. From this equation, it is evident that non-textured hydrophobic materials with $\theta_Y > 90°$ display lower adhesion to ice, in comparison to hydrophilic materials with $\theta_Y < 90°$.

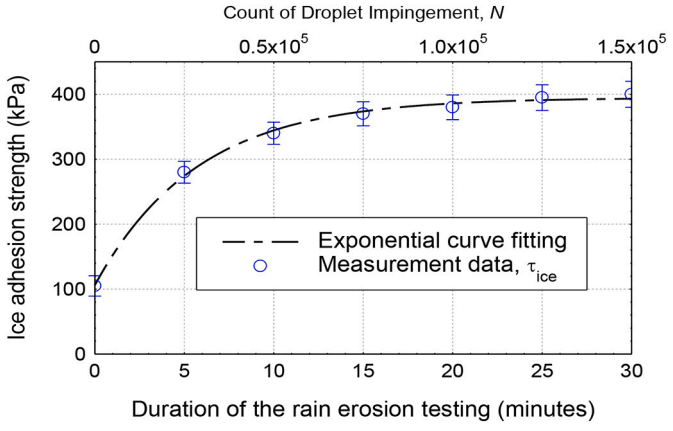

Fig. 10. Measured ice adhesion strength vs. duration of the rain erosion testing.

Based on their measurements of the ice adhesion strength on steel discs coated with fluorodecyl POSS-containing materials, Meuler et al. (2010) reported a strong correlation between the measured ice adhesion data and the receding angle of water droplets on the nominally smooth surface. More specifically, Meuler et al. (2010) suggested that the measured strength of ice adhesion, $\tau_{ice,}$ would change linearly with a contact angle scaling parameter of $[1 + \cos\theta_{rec}]$, which can be expressed as:

$$\tau_{ice} = A \cdot (1 + cos\theta_{rec}) \tag{7}$$

where A is a constant determined by the substate material, $\theta_{rec,}$ is the receding angle of water droplets on the solid surface.

More recently, Hejazi et al. (2013) investigated the parallelism between the hydrophobicity and icephobicity based on fracture mechanics theory and force balance analysis. They suggested that the main parameter affecting water droplet adhesion to a solid surface is CA hysteresis, while both receding CA and the size of voids/defects are important for the adhesion of ice particles. Hejazi et al. (2013) also suggested that ice adhesion strength to a surface can be estimated by:

$$\tau_{ice} = \sqrt{\frac{2E\gamma_{ia}(1 + cos(\theta_{rec})}{\pi a}} \tag{8}$$

where E is the Young's modulus of ice, γ_{ia} is the ice-air interaction energy, and a is the crack length. Based on the measured ice adhesion strength and the receding angle values given in Table 1, the nominal crack length of the SHS coated surface before undergoing rain erosion was estimated to be about 3 mm (i.e., $a \approx 3$ *mm*) by using the Eq. (8).

It should be noted that, after undergoing the rain erosion testing, while some of the large-scale texture/roughness structures over the SHS coated surface were found to be grinded away due to the rain erosion effects, the changes in the characteristics scales for the texture/roughness structures over the eroded SHS coated surfaces were found to be sub-micrometers (i.e., 200–300 nm as revealed quantitatively from the AFM measurement results to be discussed in the next section), which are significantly smaller than the nominal crack length of the SHS coated surface (i.e., $a \approx 3$ mm). Since the ice adhesion measurements were performed with the same test apparatus and follow a same testing procedure, the nominal crack lengths before and after the rain erosion experiments were assumed to be almost unchanged for simplicity in analyzing the measured ice adhesion strength. Therefore, the model of Hejazi et al. (2013) suggests that the measured strength of ice adhesion, $\tau_{ice,}$ would change as a square-root function against the contact angle scaling parameter of $[1 + \cos\theta_{rec}]$.

Fig. 11 gives the measured ice adhesion strength on the SHS coated test plate against the corresponding receding angle scaling parameter of $[1 + \cos\theta_{rec}]$ after different duration of the rain erosion testing. Both the empirical model suggested by Meuler et al. (2010b) (i.e., the linear function model) and the fracture mechanics model of Hejazi et al. (2013) (i.e., the square-root-law model) were used to fit the measured ice adhesion strength data, and the best-fitted curves were also given in the plot for comparison. It can be seen clearly that, the square-root-law model of Hejazi et al. (2013) was found to fit the measured ice adhesion strength data much better, in comparison to the linear-function model suggested by Meuler et al. (2010b). This can be explained by the fact that the empirical model of Meuler et al. (2010b) were actually

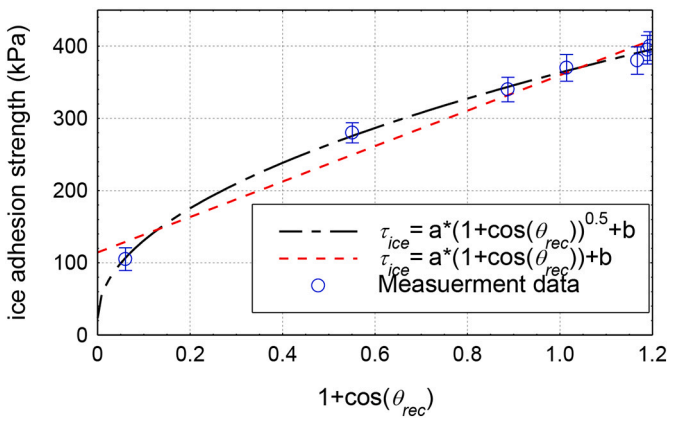

Fig. 11. Measured ice adhesion strength on the SHS coated test plate at $T_{surface}$ = −10 °C against the contact angle scaling parameter of [1 + cos θ_{rec}].

only applicable for the test cases with nominally smooth/flat surface. However, as revealed clearly from SEM images given in Fig. 2, obvious micro−/nano-textures were found to be generated over the SHS coated test surface, which will enable incident water drops to freeze in the partially wetted Cassie-Baxter state. Since the assumption of nominally smooth/flat surface used to derive the linear-function model of Meuler et al. (2010) cannot be satisfied anymore, the variation characteristics of the measured ice adhesion strength on the SHS coated test surface could not be fitted well by the linear-function model of Meuler et al. (2010).

4.4. Variations in the surface topologic characteristics of the SHS coated surface as a function of the duration of the rain erosion testing

As aforementioned, the variations in the surface topologic characteristics of the SHS coated test plate as a function of the duration of the rain erosion testing were also quantified in the present study by using an Atomic Force Microscopy (AFM) system, which can be used elucidate the underlying physics behind the experimental observations presented above. Fig. 12 shows the AFM scanned images to reveal the significant changes in the surface topology of the SHS coated test plate before and after different durations of the rain erosion experiments (i.e., after 10, 30 and 50 min of the rain erosion testing with the nominal droplet impacting speed of U_∞ = 65 m/s). Based on the quantitative AFM measurement results as those shown in Fig. 12, the key parameters to characterize surface topology, i.e., the averaged surface roughness (Ra) and the coresponding root-mean-square (Rq) values, were obtained to quantify the changes of the surface topology characteristics of the SHS coated surface due to the rain erosion effects. More specifically, the *Ra* value represents the arithmetic average of the absolute heights of the surface roughness over the test surface, i.e., $Ra = \langle h \rangle$, where h is the local height of the surface roughness. The corresponding *Rq* value represents the root-mean-square of the roughness height over the test surface, i.e., $Rq = \sqrt{\langle h^2 \rangle}$, which is used to indicate the significance of the roughness

Table 3
Measured surface roughness parameters before and after rain erosion testing.

Duration of the rain erosion testing (minutes)	0	10	30	50
Ra (nm)	562	380	369	334
Rq (nm)	775	623	573	491

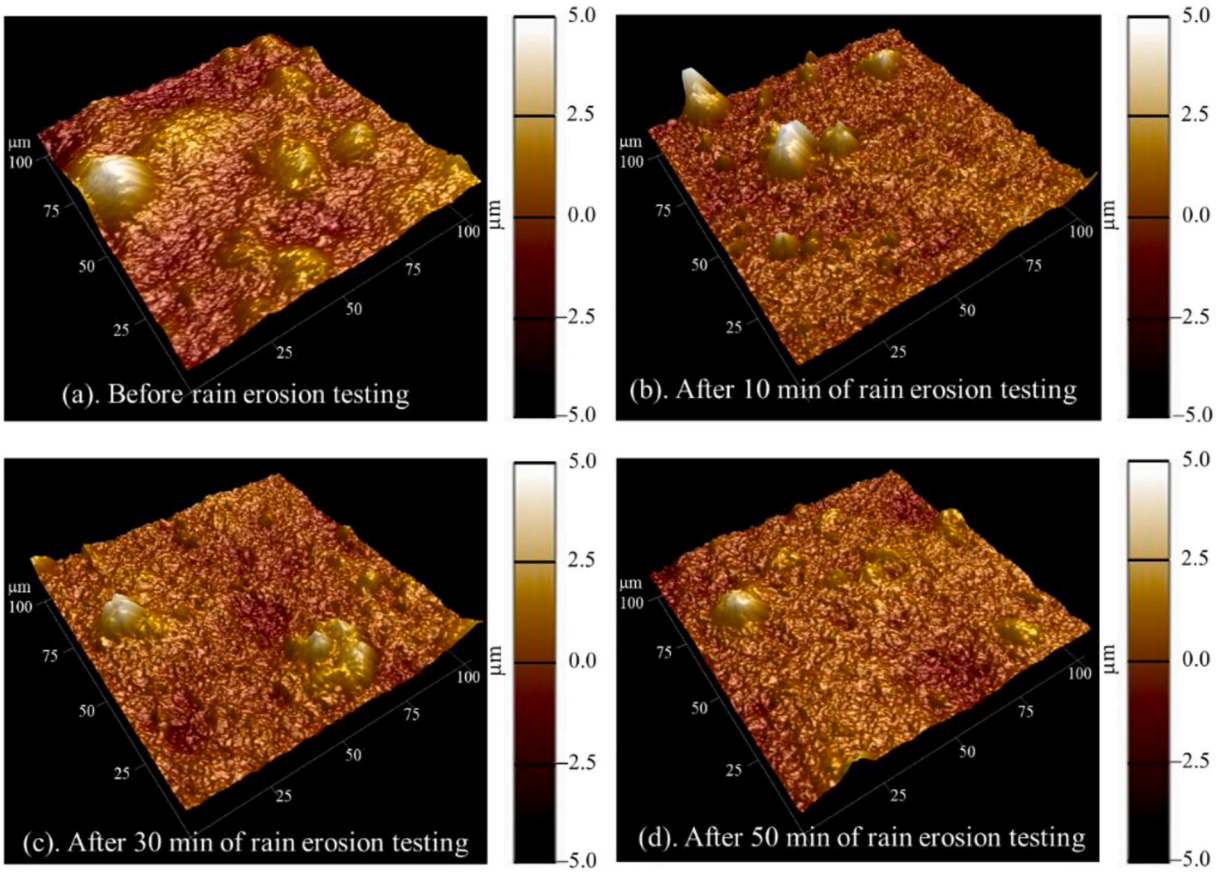

Fig. 12. Typical AFM images to reveal the changes surface topology of SHS-coated test plate after undergoing rain erosion testing with the nominal droplet impacting speed of U_∞ = 65 m/s.

peaks over the test surface. Table 3 listed the measurement data derived from the AFM images given in Fig. 12.

As shown in Fig. 12(a), obvious nano−/micro-scaled textures/roughness with different sizes and heights were found over the SHS coated test plate before conducting the rain erosion experiment (i.e., existence of hierarchical texture/roughness structures over the test surface), indicating that the SHS coated test surface is rough enough to maintain its superhydrophobicity, as expected. The corresponding surface roughness parameters were found to be $Ra = 532$ nm and $Rq = 775$ nm, As revealed clearly from the AFM images given in Fig. 4(b) to (d), after undergoing the rain erosion testing, while the texture/roughness structures with relatively smaller size and lower roughness height were still observed on the test surface, the large and sharp roughness/texture structures (i.e., textures/roughness with relatively larger size and greater roughness height) were found to be grinded away rapidly due to continuous impingement of the water droplets onto the test surface. The schematics of the rain erosion effects given in Fig. 6 can be used to explain the how the large-scale texture/roughness on the SHS coated test surface were grinded away by the impinging water droplets. Upon the dynamic impinging of the water droplets on the test plate at the impacting speed of $U_\infty = 65$ m/s, significant deformations and cracks would be initiated over the SHS coated test plate due to the extreme "water hammer pressure" generated at the initial stage of the droplet impacting process, as shown schematically in Fig. 6(a). The tremendous "water hammer pressure" (i.e., up to ~100 MPa) would smash the large and sharp roughness/textures on the SHS coated surface directly. Furthermore, the lateral water jetting effects induced by the Rayleigh surface waves as shown in Fig. 6(b) would also facilitate the tearing away of the sharp unevenness/roughness on the test surface. As a result, while the surface roughness parameters of the SHS coated test surface were found to reduce to $Ra \approx 380$ nm and $Rq \approx 623$ nm after 10 min of the rain erosion testing, the corresponding parameters become $Ra \approx 369$ and 334 nm, and $Rq \approx 573$ and 491 nm, after 30 and 60 min of the rain erosion testing, respectively. It indicates that, the SHS coated test surface would become smoother and smoother as the time of the rain erosion experiment increases. It is well known that the existence of hierarchical texture/roughness structures over the SHS coated test surface is the key to maintain its superhydrophobicity. Corresponding to the continuous grind away of the hierarchical texture/roughness structures over the test surface, the eroded SHS coated test plate was found to lose its superhydrophobicity gradually as the duration of the rain erosion testing experiment increases. Therefore, as shown quantitatively in Figs. 8 and 9, both the static CA, θ_{static}, and receding CA, θ_{rec}, were found to decrease exponentially as the duration of the rain erosion testing increases. Furthermore, due to the vanishing of the hierarchical texture/roughness structures over the SHS coated test surface, droplet waters on the test surface would be more readily to transition from the partially-wetted *Cassie-Baxter state* to the fully-wetted *Wenzel state* (Nosonovsky, 2011). Once water freezes within the surface textures in the Wenzel state, it would be very difficult to remove the ice, even more than on non-textured surfaces, because of the interlocking between ice and the textures (Lv et al., 2014; Nosonovsky and Hejazi, 2012; Sarshar et al., 2013). Consequently, as shown quantitatively in Fig. 12, the measured ice adhesion strength over the SHS coated test surface were found to increase monotonically with the increasing duration of the rain erosion testing experiments.

5. Conclusions

A comprehensive experimental investigation was conducted to evaluate the variation characteristics of the surface wettability and ice adhesion strength on a typical superhydrophobic surface (SHS) after undergoing continuous impingement of water droplets at relatively high speeds (i.e., up to ~100 m/s). The experimental study was conducted by leveraging a specially designed rain erosion testing rig available at Iowa State University to exhaust an air jet flow laden with micro-sized water droplets at different liquid water content (*LWC*) levels. The micro-sized water droplets carried by the airflow were impinging normally onto a test plates coated with a typical SHS coating to simulate the scenario with airborne, micro-sized water droplets in the cloud impacting onto airframe surfaces of an Unmanned-Aerial-System (UAS). During the experiments, the surface wettability (i.e., in terms of static, advancing and receding contact angles of water droplets siting on the test surfaces) and the resultant ice adhesion strength on the SHS coated test plate were quantified as a function of the duration of the rain erosion experiments. The evolutions of the surface topology characteristics of the SHS coated surface against the duration of the rain erosion testing were also examined quantitatively by using an Atomic Force Microscope (AFM) system.

It was found that, under the same rain erosion testing condition (i.e., with the same *LWC* level in the airflow and droplet impacting speed of U_∞), both the static contact angle (CA), θ_{static}, and the receding CA, θ_{rec}, of water droplets on the SHS coated test surface were found to decrease monotonically with the increasing duration of the rain erosion testing experiment (i.e., with more droplets impinging onto the test surface). The wettability degradation of the SHS coated surface (i.e., the decreasing rates for both the static CA, θ_{static}, and the receding CA, θ_{rec}) was found to be much faster for the test cases with higher droplet impinging speed, in comparison to those with relatively lower droplet impacting speed, as expected. The wettability degradation characteristics (i.e., the time variations for both the measured static CA, θ_{static}, and the receding CA, θ_{rec}) were found to be fitted reasonably well by using exponential functions. The ice adhesion strength on the SHS coated test plate was found to increase monotonically as the duration of the rain erosion testing increases. The variations of the resultant ice adhesion strength on the SHS coated test surface against the contact angle scaling parameter of $[1 + \cos \theta_{rec}]$ were found to be fitted well by using a square-root-law model reported in the previous study.

The variation characteristics of the surface wettability and ice adhesion strength were found to correlate well with the surface topology changes of the SHS coated test surface caused by the rain erosion effects revealed from the AFM measurement results. After undergoing the rain erosion testing, large and/or sharp roughness/texture structures on the SHS coated test surface were found to be grinded away rapidly due to the continuous droplet impinging onto the test surface. Upon the dynamic impacting of water droplets onto the test surface, both the extreme "water hammer pressure" generated at the initial stage of the droplet impacting process and the lateral jetting effects associated with the generation of Rayleigh surface waves are suggested to be responsible for tearing away of the shape roughness/unevenness on the SHS coated test surface. As a result, the SHS coated test surface was found to become smoother and smoother as the time of the rain erosion testing increases. Corresponding to the vanishing of the hierarchical texture/roughness structures on the test surface, the water droplets on the test surface would become more readily to transition from the partially-wetted *Cassie-Baxter state* to the fully-wetted *Wenzel state*, eliminating the hydrophobicity of the test surface. Therefore, both the static CA, θ_{static}, and receding CA, θ_{rec}, were found to decrease exponentially as the duration of the rain erosion experiment increases. Furthermore, once water freezes within the surface textures in the Wenzel state, it would be very difficult to remove the ice, because of the interlocking between ice and the textures. As a result, the ice adhesion strength over the eroded SHS coated test surface were found to increase monotonically with the increasing duration of the rain erosion testing experiment.

While the primary objective of the present study is to characterize the wettability degradation of SHS coatings induced by the rain erosion effects, rain erosion effects would also induce surface damages to the other state-of-the-art icephobic coatings (e.g., pitcher-plant-inspired slippery liquid-infused porous surfaces (SLIPS) or elastic soft materials/surfaces) as well as bare metal surfaces. A set of comprehensive experimental campaigns will be conducted in the near future to examine rain erosion effects on surface topology changes and wettability

degradations of various state-of-the-art icephobic coatings, in comparison to those of metal surfaces, for the development of more effective and robust anti−/de-icing strategies tailored specifically for UAS inflight icing mitigation.

Declaration of Competing Interest

The authors declare that they have no known competing financial interests or personal relationships that could have appeared to influence the work reported in this paper.

Acknowledgments

The research work is partially supported by Iowa Space Grant Consortium (ISGC) Base Program for Aircraft Icing Studies, National Aeronautics and Space Administration (NASA) with the grant number of NNX16AN21A, and National Science Foundation (NSF) under award numbers of CMMI- 1824840 and CBET- 1916380.

References

Antonini, C., Innocenti, M., Horn, T., 2011. Understanding the effect of superhydrophobic coatings on energy reduction in anti-icing systems. Cold Reg. Sci. Technol. 67, 58–67.

Antonini, C., Villa, F., Marengo, M., 2014. Oblique impacts of water drops onto hydrophobic and superhydrophobic surfaces: outcomes, timing, and rebound maps. Exp. Fluids 55, 1713. https://doi.org/10.1007/s00348-014-1713-9.

Beemer, D.L., Wang, W., Kota, A.K., 2016. Durable gels with ultra-low adhesion to ice. J. Mater. Chem. A 4, 18253–18258. https://doi.org/10.1039/c6ta07262c.

Beeram, P.S.R., Waldman, R.M., Hu, H., 2017. Measurements of Ice Adhesion over Ice Mitigation Coatings Pertinent to Aircraft Icing and Anti−/De-Icing, in: 9th AIAA Atmospheric and Space Environments Conference. American Institute of Aeronautics and Astronautics, Reston, Virginia. https://doi.org/10.2514/6.2017-3928.

Blowers, R.M., 1969. On the response of an elastic solid to droplet impact. IMA J. Appl. Math. 5, 167–193.

Botura, G., Fahrner, A., 2003. Icing detection system - Conception, development, testing and applicability to UAVS. In: 2nd AIAA "Unmanned Unlimited" Conference and Workshop and Exhibit. https://doi.org/10.2514/6.2003-6637.

Brown, J.M., Raghunathan, S., Watterson, J.K., Linton, A.J., Riordon, D., 2002. Heat transfer correlation for anti-icing systems. J. Aircr. 39 https://doi.org/10.2514/2.2896.

Cao, L., Jones, A.K., Sikka, V.K., Wu, J., Gao, D., 2009. Anti-icing superhydrophobic coatings. Langmuir 25, 12444–12448. https://doi.org/10.1021/la902882b.

Cao, Y., Tan, W., Wu, Z., 2018. Aircraft icing: an ongoing threat to aviation safety. Aerosp. Sci. Technol. https://doi.org/10.1016/j.ast.2017.12.028.

Cassie, A., Baxter, S., 1944. Wettability of porous surfaces. Trans. Faraday Soc. 40, 546–551.

Dear, J.P., Field, J.E., 1988. High-speed photography of surface geometry effects in liquid/solid impact. J. Appl. Phys. 63, 1015–1021. https://doi.org/10.1063/1.340000.

Deng, X., Mammen, L., Butt, H., Vollmer, D., 2012. Candle soot as a template for a transparent robust superamphiphobic coating. Science (80-.) 335, 67–70.

Dorrer, C., Rühe, J., 2009. Some thoughts on superhydrophobic wetting. Soft Matter 5, 51. https://doi.org/10.1039/b811945g.

Feng, L., Li, S., Li, Y., Li, H., Zhang, L., Zhai, J., Song, Y., Liu, B., Jiang, L., Zhu, D., 2002. Super-hydrophobic surfaces: from natural to artificial. Adv. Mater. 14, 1857–1860. https://doi.org/10.1002/adma.200290020.

Fujisawa, N., Takano, S., Fujisawa, K., Yamagata, T., 2018. Experiments on liquid droplet impingement erosion on a rough surface. Wear 398–399, 158–164. https://doi.org/10.1016/j.wear.2017.12.003.

Gao, L., Liu, Y., Ma, L., Hu, H., 2019. A hybrid strategy combining minimized leading-edge electric-heating and superhydro−/ice-phobic surface coating for wind turbine icing mitigation. Renew. Energy 140, 943–956. https://doi.org/10.1016/J.RENENE.2019.03.112.

Ghidaoui, M.S., Zhao, M., McInnis, D.A., Axworthy, D.H., 2005. A review of water hammer theory and practice. Appl. Mech. Rev. 58, 49. https://doi.org/10.1115/1.1828050.

Grundwürmer, M., Nuyken, O., Meyer, M., Wehr, J., Schupp, N., 2007. Sol–gel derived erosion protection coatings against damage caused by liquid impact. Wear 263, 318–329. https://doi.org/10.1016/J.WEAR.2006.12.039.

Hejazi, V., Sobolev, K., Nosonovsky, M., Rohatgi, P.K., 2013. From superhydrophobicity to icephobicity: forces and interaction analysis. Sci. Rep. 3, 70–71. https://doi.org/10.1038/srep02194.

Heyman, F., 1970. Erosion by liquids. In: Machine Design, pp. 118–124.

Jackson, M.J., Field, J.E., 2000. Modelling liquid impact fracture thresholds in brittle materials. Br. Ceram. Trans. 99, 1–13. https://doi.org/10.1179/bct.2000.99.1.1.

Korhonen, J.T., Huhtamäki, T., Ikkala, O., Ras, R.H.A., 2013. Reliable measurement of the receding contact angle. Langmuir 29, 3858–3863. https://doi.org/10.1021/la400009m.

Kulinich, S.A., Farzaneh, M., 2011. On ice-releasing properties of rough hydrophobic coatings. Cold Reg. Sci. Technol. 65, 60–64. https://doi.org/10.1016/j.coldregions.2010.01.001.

Li, X.-M., Reinhoudt, D., Crego-Calama, M., 2007. What do we need for a superhydrophobic surface? A review on the recent progress in the preparation of superhydrophobic surfaces. Chem. Soc. Rev. 36, 1350–1368. https://doi.org/10.1039/b602486f.

Liu, Y., Bond, L.J., Hu, H., 2017. Ultrasonic-attenuation-based technique for ice characterization pertinent to aircraft icing phenomena. AIAA J. 1–8. https://doi.org/10.2514/1.J055500.

Liu, Y., Li, L., Li, H., Hu, H., 2018. An experimental study of surface wettability effects on dynamic ice accretion process over an UAS propeller model. Aerosp. Sci. Technol. 73, 164–172. https://doi.org/10.1016/J.AST.2017.12.003.

Lv, J., Song, Y., Jiang, L., Wang, J., 2014. Bio-inspired strategies for anti-icing. ACS Nano 8, 3152–3169. https://doi.org/10.1021/nn406522n.

Ma, L., Zhang, Z., Gao, L., Liu, Y., Hu, H., 2020. Bio-inspired icephobic coatings for aircraft icing mitigation: a critical Review. Rev. Adhes. Adhes. 8, 168–199. https://doi.org/10.7569/RAA.2020.097307.

Maitra, T., Tiwari, M.K., Antonini, C., Schoch, P., Jung, S., Eberle, P., Poulikakos, D., 2014. On the nanoengineering of superhydrophobic and impalement resistant surface textures below the freezing temperature. Nano Lett. 14, 172–182. https://doi.org/10.1021/nl4037092.

Makkonen, L., 1997. Surface Melting of Ice. J. Phys. Chem. B 101, 6196–6200. https://doi.org/10.1021/JP963248C.

Makkonen, L., 2012. Ice adhesion—theory, measurements and countermeasures. J. Adhes. Sci. Technol. 26, 413–445.

Meuler, A.J., Smith, J.D., Varanasi, K.K., Mabry, J.M., McKinley, G.H., Cohen, R.E., 2010. Relationships between Water Wettability and Ice Adhesion. ACS Appl. Mater. Interfaces 2, 3100–3110. https://doi.org/10.1021/am1006035.

Mishchenko, L., Hatton, B., Bahadur, V., 2010. Design of ice-free nanostructured surfaces based on repulsion of impacting water droplets. ACS Nano 4 (12), 7699–7707.

Miziński, B., Niedzielski, T., 2017. Fully-automated estimation of snow depth in near real time with the use of unmanned aerial vehicles without utilizing ground control points. Cold Reg. Sci. Technol. 138, 63–72. https://doi.org/10.1016/j.coldregions.2017.03.006.

Mollaeian, K., Liu, Y., Bi, S., Ren, J., 2019. Investigation of the effect of substrate morphology on MDCK cell mechanical behavior using atomic force microscopy. Appl. Phys. Lett. 115, 063701 https://doi.org/10.1063/1.5109115.

Muthumani, A., Fay, L., Akin, M., Wang, S., Gong, J., Shi, X., 2014. Correlating lab and field tests for evaluation of deicing and anti-icing chemicals: a review of potential approaches. Cold Reg. Sci. Technol. 97, 21–32. https://doi.org/10.1016/j.coldregions.2013.10.001.

Nosonovsky, M., 2011. Materials science: Slippery when wetted. Nature 477, 412–413. https://doi.org/10.1038/477412a.

Nosonovsky, M., Hejazi, V., 2012. Why superhydrophobic surfaces are not always icephobic. ACS Nano 6, 8488–8491. https://doi.org/10.1021/nn302138r.

Parent, O., Ilinca, A., 2011. Anti-icing and de-icing techniques for wind turbines: critical review. Cold Reg. Sci. Technol. 65, 88–96. https://doi.org/10.1016/j.coldregions.2010.01.005.

Saleema, N., Farzaneh, M., Paynter, R.W., Sarkar, D.K., 2011. Prevention of ice accretion on aluminum surfaces by enhancing their hydrophobic properties. J. Adhes. Sci. Technol. 25, 27–40. https://doi.org/10.1163/016942410X508064.

Sarshar, M.A., Swarctz, C., Hunter, S., Simpson, J., Choi, C.-H., 2013. Effects of contact angle hysteresis on ice adhesion and growth on superhydrophobic surfaces under dynamic flow conditions. Colloid Polym. Sci. 291, 427–435. https://doi.org/10.1007/s00396-012-2753-4.

Sharifi, N., Dolatabadi, A., Pugh, M., Moreau, C., 2019. Anti-icing performance and durability of suspension plasma sprayed TiO2 coatings. Cold Reg. Sci. Technol. 159, 1–12. https://doi.org/10.1016/j.coldregions.2018.11.018.

Slot, H.M., Gelinck, E.R.M., Rentrop, C., Van der Heide, E., 2015. Leading edge erosion of coated wind turbine blades: Review of coating life models. Renew. Energy 80, 837–848. https://doi.org/10.1016/j.renene.2015.02.036.

Tarquini, S., Antonini, C., Amirfazli, A., Marengo, M., Palacios, J., 2014. Investigation of ice shedding properties of superhydrophobic coatings on helicopter blades. Cold Reg. Sci. Technol. 100, 50–58. https://doi.org/10.1016/j.coldregions.2013.12.009.

Thomas, G.P., Brunton, J.H., 1970. Drop impingement erosion of metals. Proc. R. Soc. A Math. Phys. Eng. Sci. 314, 549–565. https://doi.org/10.1098/rspa.1970.0022.

Thomas, S.K., Cassoni, R.P., MacArthur, C.D., 1996. Aircraft anti-icing and de-icing techniques and modeling. J. Aircr. 33, 841–854. https://doi.org/10.2514/3.47027.

Tourkine, P., Le Merrer, M., Quéré, D., 2009. Delayed freezing on water repellent materials. Langmuir 25, 7214–7216. https://doi.org/10.1021/la900929u.

Valaker, E.A., Armada, S., Wilson, S., 2015. Droplet Erosion Protection Coatings for Offshore Wind Turbine Blades, Energy Procedia. Elsevier B.V. https://doi.org/10.1016/j.egypro.2015.11.430.

Varanasi, K., Deng, T., Smith, J., 2010. Frost formation and ice adhesion on superhydrophobic surfaces. Appl. Phys. Lett. 97, 8234102.

Xie, S., Ren, J., 2019. High-speed AFM imaging via iterative learning-based model predictive control. Mechatronics 57, 86–94. https://doi.org/10.1016/j.mechatronics.2018.11.008.

Yao, X., Song, Y., Jiang, L., 2011. Applications of bio-inspired special wettable surfaces. Adv. Mater. 23, 719–734.

Yeong, Y.H., Burton, J., Loth, E., Bayer, I.S., 2014. Drop impact and rebound dynamics on an inclined superhydrophobic surface. Langmuir 30, 12027–12038. https://doi.org/10.1021/la502500z.

Zhang, B., Tang, L., Roemer, M., 2014. Probabilistic weather forecasting analysis for unmanned aerial vehicle path planning. J. Guid. Control. Dyn. 37, 309–312. https://doi.org/10.2514/1.61651.

Zografi, G., Johnson, B.A., 1984. Effects of surface roughness on advancing and receding contact angles. Int. J. Pharm. 22, 159–176. https://doi.org/10.1016/0378-5173(84)90019-X.